iScience

CellPress
OPEN ACCESS

Article

Deployable vortex generators for low Reynolds numbers applications powered by cephalopods inspired artificial muscles

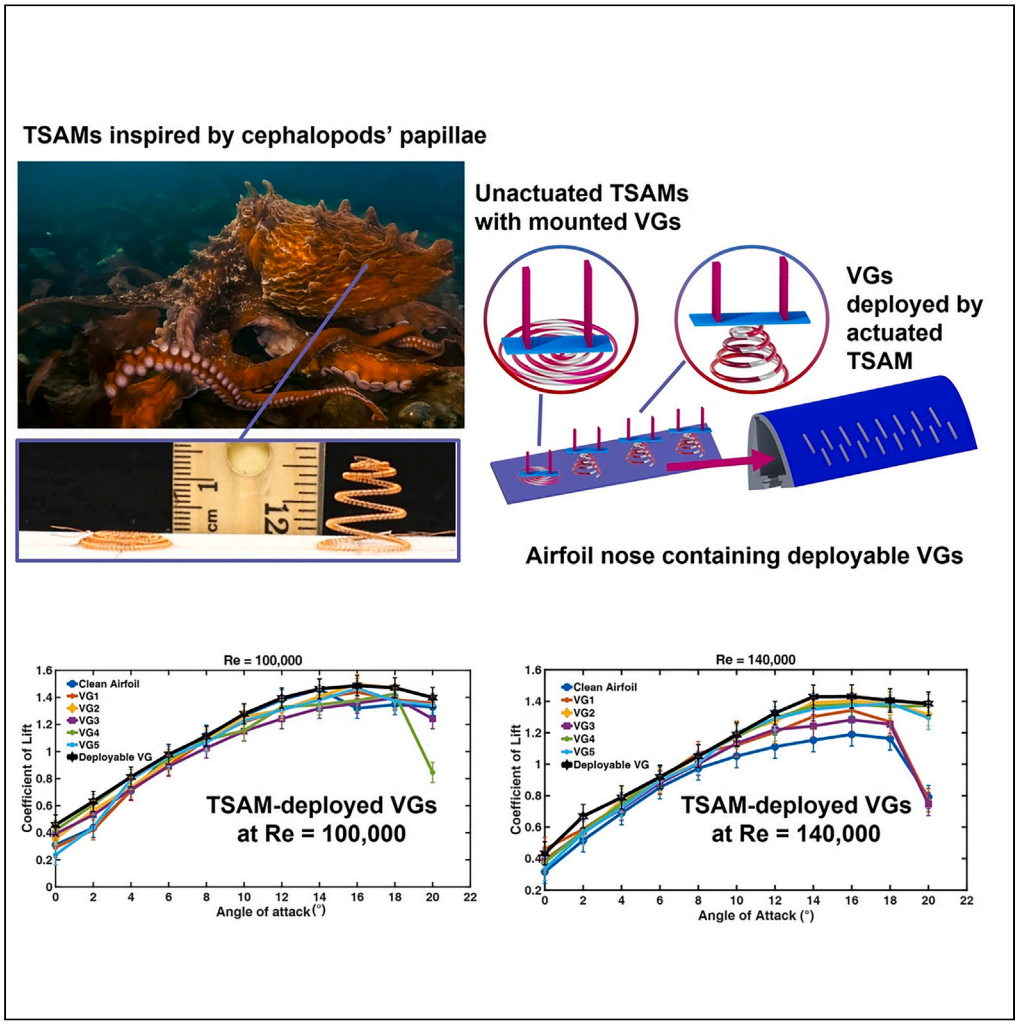

Rabiu Mamman, Parth Kotak, Thilina Weerakkody, Tatum Johnson, Austin Krebill, James Buchholz, Caterina Lamuta

caterina-lamuta@uiowa.edu

Highlights

A bioinspired active flow control device was proposed

The proposed device is powered by twisted spiral artificial muscles (TSAMs)

The device was tested in a wind tunnel at Reynolds numbers between 100,000 and 140,000

Test results showed that the device improved aerodynamic performance of the wing

Mamman et al., iScience *26*, 108369
December 15, 2023
https://doi.org/10.1016/j.isci.2023.108369

iScience

CellPress
OPEN ACCESS

Article

Deployable vortex generators for low Reynolds numbers applications powered by cephalopods inspired artificial muscles

Rabiu Mamman,[1] Parth Kotak,[1] Thilina Weerakkody,[1] Tatum Johnson,[1] Austin Krebill,[1] James Buchholz,[1] and Caterina Lamuta[1,2,*]

SUMMARY

This paper proposes deployable vortex generators (VGs) powered by twisted spiral artificial muscles (TSAMs). TSAMs take inspiration from cephalopods' papillae and can protrude out of plane upon electro-thermal actuation with an output strain of 2000% and an input voltage of 0.2 V/cm. Unlike passive VGs, designed for specific flow conditions, this technology can adjust to changes in flow conditions by overcoming the limitations of existing active flow control devices in terms of portability and power requirements. Our technology can deploy different VGs configurations on demand, and match a desired target configuration, optimized for a specific flow condition. Experiments were conducted in a wind tunnel using a NASA Langley Research Center LS (1)-0417 GA(W)-1 airfoil. Stall delays and lift increase have been demonstrated for different flow conditions, with Reynolds numbers between 100,000 and 140,000. These findings are promising for enhancing efficiency in small unmanned aerial vehicles operating at low Reynolds numbers.

INTRODUCTION

Small unmanned aerial vehicles (UAVs) have gained widespread interest in recent years owing to their versatility, maneuverability, and endurance. They are particularly valuable for real-time reconnaissance in high-risk areas and operations in challenging environments such as border patrol, wildlife management, and search and rescue missions.[1–3] These UAVs usually operate at high altitudes and low Reynolds numbers, which are often less than 200,000 as shown in Figure 1A.[4] At low Reynolds numbers, the main challenge for small UAVs is the occurrence of laminar flow separation. When Reynolds numbers fall below 200,000, the laminar boundary layers close to the leading edge of the airfoil tend to separate due to the formation of an adverse pressure gradient. This leads to the formation of a laminar separation bubble (LSB) between the separation and reattachment points, which adversely affects the aerodynamic behavior of the airfoil. Laminar flow separation significantly reduces lift and increases drag, which results in a decrease in the lift-drag ratio and, in some cases, aerodynamic stall.[5]

One common method to enhance the performance of airfoils operating at low Reynolds numbers is to induce turbulent flow by tripping the boundary layer. Turbulent flow promotes reattachment of the flow after separation by mixing low and high momentum flow.[6] Figure 1B[4] illustrates the aerodynamic performance of 'smooth' and 'rough' airfoils at low Reynolds numbers. The graph shows that 'smooth' airfoils experience a low lift/drag (L/D) ratio when the Reynolds number is less than 100,000 due to the presence of the LSB.[1–3] On the other hand, 'rough' airfoils do not exhibit the same behavior because the flow transitions to a turbulent regime, which re-energizes the flow and resists separation.

In order to mitigate the problems of flow separation, static vortex generators (VGs) have been widely used to promote boundary-layer transition.[7] The use of VGs is widespread because they offer cost-effective and easy-to-design solutions.[8] VGs can be fabricated in different shapes, including rectangular, triangular, trapezoidal wishbone, doublet, wedge, ramp, and numerous others.[9] Different shapes of VGs can yield to different separation suppression modes due to the varying strength of their vortices.

The geometry and position of VGs need to be optimized to suite different flow conditions. Specifically, the efficiency of VGs is greatly influenced by their position with respect to the leading edge of an airfoil, spanwise spacing, and their height in relation to the boundary layer thickness.[10] The chordwise position of a VG can be expressed using the dimensionless parameter, x/c where x is the position of the VG along the chord and c is the chord length. When VGs are placed too close to the leading edge, they can generate vortices that disrupt incoming flow thereby causing premature flow separation and reduce lift generation. Conversely, when the VGs are too far downstream, the flow might separate before reaching the VGs. Generally, a value of x/c between 0.2 and 0.3 has been found to provide the best performance in terms of lift increment and stall delay.[11,12] VG height must be chosen to avoid drag increase.[13–15] Conventional VGs are usually characterized by $h/\delta \geq 1$ where h is the VG height and δ is the thickness of the boundary layer. Finally, concerning VGs orientation, they can be placed in a

[1]Department of Mechanical Engineering, University of Iowa, Iowa City, IA 52242, USA
[2]Lead contact
*Correspondence: caterina-lamuta@uiowa.edu
https://doi.org/10.1016/j.isci.2023.108369

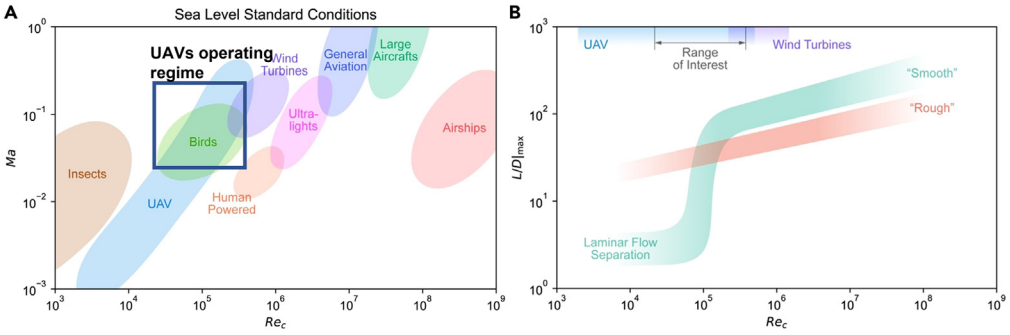

Figure 1. Reynolds number ranges for different aerial vehicles

(A) Reynolds number operating regime for various aircrafts including UAVs under sea level standard conditions.

(B) Effect of Reynolds numbers on maximum L/D ratio for smooth and rough airfoils.[4] *Adapted with permission from Lissaman, P B S Annual Review of Fluid Mechanics, 31 Dec 1982, Vol. 15, Issue 1, pages 223–239. Copyright 1983 by Annual Reviews Inc.

co-rotating manner such that each VG is oriented in the same direction, or a counter-rotating manner where VGs in a pair have different orientations.[7,16]

It has been demonstrated that each VG orientation offers several advantages over the other.[17–19] The counter-rotating VG orientation generates vortices that promote more efficient mixing of fluid streams compared to co-rotating vortices. Since counter-rotating vortices are characterized by two or more vortices rotating in opposite directions, when such vortices are formed, the opposing rotation directions of the vortices results in the formation of a higher-pressure regions between them which results in the generation of additional lift. The co-rotating VG orientation tends to generate vortices that are more coherent than the counter-rotating VG orientation. In terms of VG layout, single or multiple row arrays of VGs have been adopted in several studies. The advantages of single or multiple rows however depend on specific flow conditions.[20–22]

Since conventional static VGs are passive flow control devices, they are not able to adapt to different flow regimes, characterized by large variations in the Reynolds numbers. Several active devices for flow controls have been proposed in the literature. This includes synthetic jet and plasma actuators, fluid oscillators, jet flaps, microelectromechanical systems and pulse blowing devices.[23–26] Active devices can adjust to changes in flow conditions, reduce parasitic drag, and delay stalls while increasing the lift coefficient. Synthetic jet actuators and dielectric barrier discharge (DBD) plasma actuators represent the most researched devices for active flow controls. The application of synthetic jet actuators is mainly limited by their power consumptions since they rely on oscillating membranes that require consistent supply of power for actuation. Moreover, piezoelectrically driven synthetic jets are characterized by low orifice velocities which are undesirable for applications where significant flow manipulations are required.[27] DBD plasma actuators have been widely employed in controlling flow separation. Apart from high voltage requirements, they are also limited to relatively low Reynolds number range, due to weak induced flow generated by the plasma.[28] In general, the need for multiple and bulk components for operation, and high-power requirements represent common drawbacks for all active devices for flow controls proposed so far, by hampering their integration into the wings of small UAVs.

Besides purely passive and active VGs, deployable VGs have also been proposed in the literature.[29–31] These solutions deploy static VGs on demand, using hydraulic actuators,[29] or shape memory alloy actuators.[30,31] Although stall delay was demonstrated in these works, the proposed solutions are still limited in terms of portability and controllability, considering the high volume and weight of hydraulic actuators, and the highly hysterestic behavior of shape memory alloys, respectively.

In this study, deployable VGs powered by bioinspired twisted spiral artificial muscles (TSAMs) are proposed for improving the aerodynamic performance of small UAVs operating at low Reynolds numbers (i.e., lower than 200,000). TSAMs can mimic the dynamic behavior of the papillae muscles of cephalopods under electrothermal actuation.[32] Figure 2A shows the activation of papillae in the cuttlefish,[33,34] while Figure 2C shows papillae in the octopus.[35] Cephalopods use papillae to change the texture of their skin to camouflage or adapt their hydrodynamic performance while swimming.[35–37] While TSAMs do not mimic the materials structure and working mechanism of papillae muscles (based on the interplay between muscular structure and hydrostatic pressure[35–37]), they take inspiration from cephalopods' papillae to produce a large out-of-plane vertical displacement upon actuation. They are manufactured by twisting inexpensive polymer fishing lines and are coiled to form Archimedean spirals. When electrothermally actuated, TSAMs undergo reversible extensions exceeding 2000% strain (see Figure 2B) within a few seconds, with an input voltage of only 0.2 V/cm. In previous works, we proposed theoretical models[32,38] and different manufacturing methods[32,36,39] for TSAMs, and we also demonstrated that TSAMs are promising candidates for the development of fouling release devices.[40] In this work, we demonstrate how TSAMs can be used to actively deploy VGs, by emulating cephalopods' papillae in terms of flow controls. Thanks to their ease of manufacturing, low specific cost, low actuation voltage requirements, large output displacement, high specific power, non-hysteretic behavior, and their compact, lightweight, and single-component nature,[41] TSAMs can effectively address the limitations of existing active flow control and deployable VGs devices in terms of power requirements, portability, ease of integration, and controls.

In this study, rectangular vane VGs are deployed on-demand by TSAMs actuation in response to changes in the flow conditions. The fabrication and design of the proposed setup is first described. Lift measurements are then reported for the airfoil operating at two different

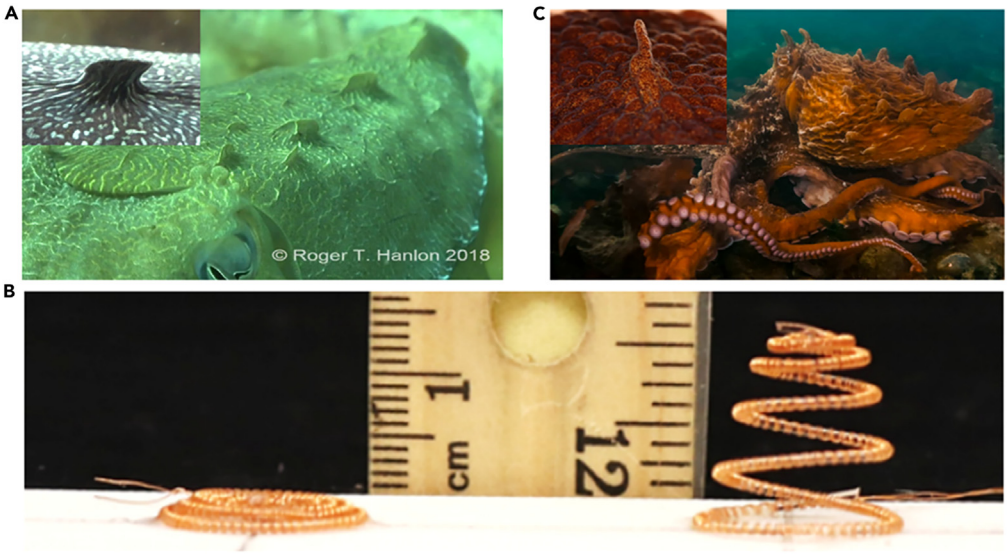

Figure 2. Cephalopods and cephalopods inspired papillae muscles

(A) Cuttlefish with actuated papillae muscles (inset showing protrusion of a single papillae).

(B) Out of plane vertical actuation of a TSAM (left: flat configuration before actuation; right: actuated configuration upon electrothermal input).

(C) Octopus with actuated papillae muscles (inset showing protrusion of a single papillae).

Reynolds numbers with and without passive VGs. Finally, passive VGs are mounted to electrothermally actuated TSAMs and the corresponding lift measurements are compared with the purely passive case to demonstrate that TSAMs can deploy different VGs configurations on demand, to provide optimal performance under different flow conditions. This approach stands out due to its affordability, minimal component requirements, ease of integration, and low power requirement. Our solution can be considered a hybrid technology between static and dynamic devices for flow control, and it is able to combine the advantages of static and dynamic solutions by proposing adaptive and compact deployable VGs.

RESULTS

Performance of passive VGs

Experimental tests using static passive VGs were first performed to identify the best VGs configuration for different flow conditions. Figure 3A shows a plot of lift coefficient versus angles of attack at Re = 100,000. The lift coefficient C_L is defined as:

$$C_L = \frac{L}{1/2\,\rho U^2 A} \quad \text{(Equation 1)}$$

where ρ is the air density, U is the free stream velocity, A is the wing area.

For the clean airfoil (dark blue curve in Figures 3A and 3B) the onset of stall can be observed at an angle of 14° and all passive VGs configurations seem to delay the onset of stall to larger angles of attack. The VG 1, VG 2, and VG 5 configurations appear to delay stall until

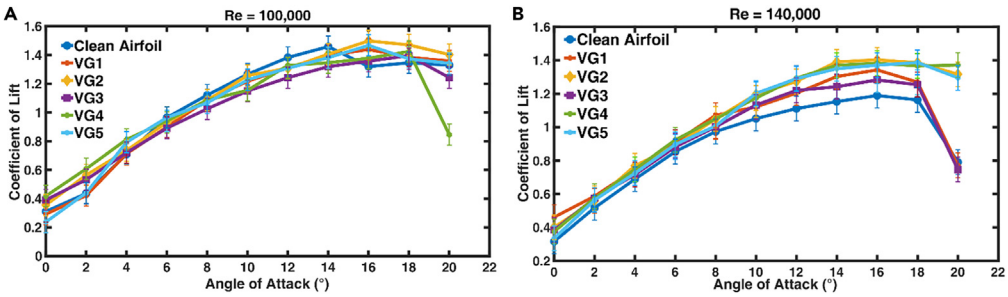

Figure 3. Effects of passive VGs on the coefficient of lift of the airfoil at different angles of attack

(A) Reynolds number 100,000 (B) Reynolds number of 140,000.

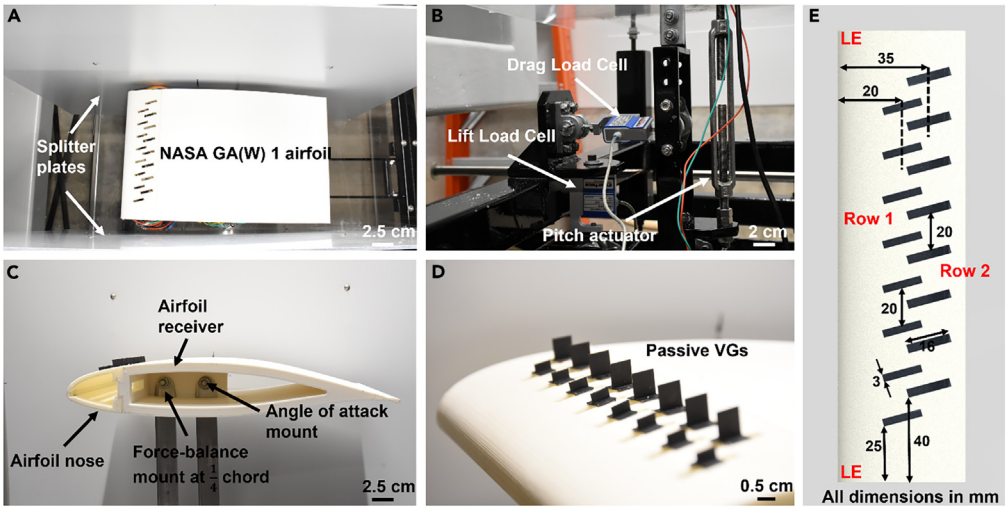

Figure 4. Experimental setup in the wind tunnel

(A) Wing model mounted in the wind tunnel with splitter plates to simulate quasi 2D-flow.

(B) Two-axis force balance system and pitch actuator used for changing the angle of attack of the airfoil.

(C) Two-piece airfoil design with a detachable nose section. Airfoil is mounted to the force-balance system at the quarter-chord point.

(D) Passive VGs affixed in two rows to the airfoil nose.

(E) VG spacing and distance from the LE of the airfoil.

16° while significant delay was recorded for VG3 and VG4 at 18°. In terms of lift generation, it was observed that VG2, VG3, and VG4 generates more lift than the clean airfoil at angles of attack between 0 and 5° degrees while the clean airfoil generates more lift between 6° up until the stall angle. A strong stall was experienced with VG4 configuration, which can be attributed to the inability of the configuration to maintain attached flow. Similar results for similar VGs configurations have been observed in previous study.[15] It is also worth noting that the double rows layout (VG2, VG4, and VG5) configurations outperformed the single rows configuration (VG1 and VG3). This outcome also aligns with results from previous studies.[42,43]

Figure 3B depicts the aerodynamic performance of the clean airfoil compared to the various VG layout and configurations at Re = 140,000. It can be observed that all VGs configurations performed better than the clean airfoil in terms of lift generation. The best performing configuration (VG2) in-terms of lift generation at Re = 140,000, increases the lift coefficient by 19% compared to the clean airfoil. These observed trends are in compliance with previous studies on effect of VGs on the aerodynamic performance of wings.[16,44–46] It was also observed that at angles of attack between 10 and 20° , lift coefficient with the two-row layout of VGs (VG2, VG4, and VG5) are higher than with single row layout. This effect can be attributed to the ability of the double row layout to hold the flow in place even as the angle of attack increases thereby preventing total stall. This observation also agrees with results from.[42]

Notably, at a Reynolds number of 100,000, the clean airfoil produces the highest lift for angles of attack between 8 and 14°. Moreover, at the same angle of attack, different VG configurations have distinct impacts on the airfoil's performance at the two Reynolds numbers tested. These findings demonstrate the significance of VGs in enhancing aerodynamic performance and highlight the importance of carefully selecting the appropriate VG configuration for a given Reynolds number and angle of attack. It is important to acknowledge that the lift measurements, as illustrated in Figures 3A and 3B, may contain intrinsic uncertainties. Uncertainties in lift measurements in the wind tunnels are commonly associated with difference in flow conditions, test model geometries, wind tunnel type and measurement methods.[47] In this study, repeated trials with identical experimental setup were carried out in the wind tunnel which can exhibit scatter in the experimental data. Moreover, noise and vibrations from the wind tunnel could have affected the sensitivity of the force balance and caused fluctuations in measurements. In order to the mitigate this to the barest minimum, low pass filtering and band-pass techniques as specified in the signal conditioner operation manual were used to reduce random fluctuations and as-well eliminate noises that falls outside the range of interest for the lift force measurements.

Impact of airfoil nose grooves on lift and stall

The airfoil initially designed to test the static VGs does not have grooves on the nose section. However, grooves were added to the airfoil for the dynamic device (see Figure 4A) to facilitate the protrusion of the TSAM-powered VGs into the flow path upon actuation. Considering that small amplitude disturbances on the surface could excite separation bubble instabilities and thereby alter the separation behavior over the airfoil,[48] we find it necessary to ascertain aerodynamic performance by conducting a comparative testing between the airfoil with grooves and the airfoil without grooves. Figures 5A and 5B shows a plot of lift coefficient versus the angle of attack in both scenario at Re = 100,000 and 140,000.

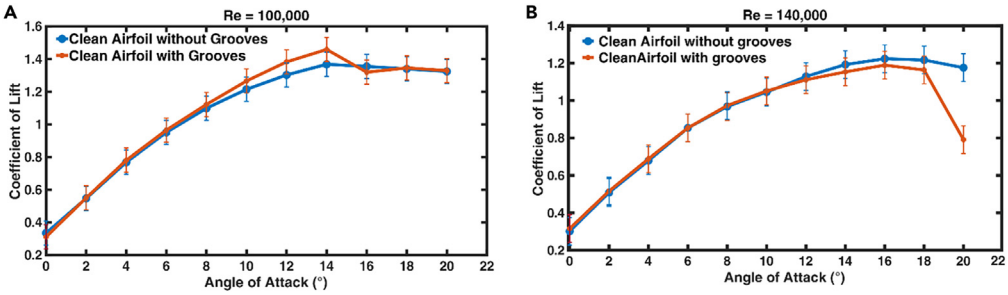

Figure 5. Coefficient of lift vs. angle of attack for a clean airfoil with and without grooves
(A) Reynolds number of 100,000 (B) Reynolds number of 140,000.

As depicted in Figure 5A, the clean airfoil with grooves generates 6% higher maximum lift coefficient compared to the airfoil without grooves at a stall angle of 14°. This can be partly attributed to the ability of the surface grooves to eliminate LSB, thereby improving the aerodynamic performance at angle of attack near the stall point, as observed in.[49] In this study[49] Liu et al. investigated 2D flow around a NACA 4415 airfoil with surface grooves closer to the leading edge. It was observed that surface grooves with optimal parameters can improve the aerodynamic lift of the wing near the stall angle by 50% compared to the baseline. However, in our tests the difference in lift coefficient was not that significant. Moreover, at a Reynolds number of 140,000 and a stall angle of 16° the clean airfoil without grooves generates a 2.5% higher peak lift as compared to the airfoil with grooves (Figure 5A). These differences between our results and results in[49] can be attributed to a different airfoil geometry. Results in Figure 5 show then that the lift profile for the two-piece airfoil with grooves does not perfectly match that of the clean airfoil for all angles of attack and Reynolds numbers tested. However, these differences are lower than 6% for angles of attack between 0 and 18. Studying the physical reasons behind such differences is out of the scope of this work, which focuses on proposing an active flow control device able to produce different static VGs configurations to improve the performance of a clean airfoil under different flow conditions.

Performance of active VGs deployed by TSAMs

The main goal of this study is to determine if the on-demand deployment of the TSAM-powered VGs can match the peak performance of different VG configurations corresponding to different angles of attack. As previously discussed, each TSAM powers two VGs. Since there are 8 VGs in each row, 4 TSAMs are placed in each row of the insert plate (Figure 6B) at the same distance from the leading edge corresponding to the VG configuration. For a given Reynolds number, the TSAM-powered VGs were selectively actuated to match the peak values of the coefficient of lift provided by different VGs configuration for different angles of attack. Tables 1 and 2 depict the corresponding VG configurations deployed at each angle of attack when testing the dynamic device at Reynolds number of 100,000 and 140,000, respectively. Each VG configurations was deployed at the maximum height of the VG element (i.e., 2 mm or 8 mm, as described in the caption of the second table in the method details section).

As shown in Figures 7A and 7B, the black curve depicts the performance of the TSAM-powered VGs. The effects of the active VGs powered by TSAMs at a Reynolds number of 100,000 are shown in Figure 7A. It can be observed from the black curve that the TSAM-powered VG

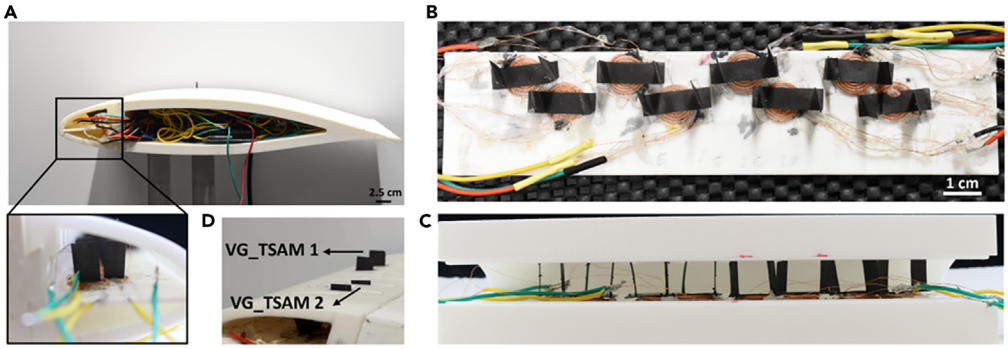

Figure 6. Pictures of the manufactured airfoil with TSAMs-powered VGs
(A) Airfoil section with the deployable VGs (shown in the inset) and electrical setup for actuating TSAMs.
(B) Top view of the TSAMs powered VGs mounted on an insert plate that can be slotted into the nose of the airfoil.
(C) Side view of the TSAMs powered VGs inside the airfoil nose.
(D) Deployable VGs powered TSAM protruding out of the nose groove upon controlled actuation (VG_TSAM 1: 8mm and VG_TSAM 2: 2mm).

Table 1. Angles of attack Vs. VG configuration deployed at Re = 100,000

Angles of attack in degrees (°)	Configuration deployed for TSAM powered VGs
0	VG4
2	VG4
4	VG4
6	VG5
8	CA
10	CA
12	CA
14	CA
16	VG2
18	VG2
20	VG2

CA, clean airfoil.

configuration follows the path of maximum lift for the entire range of angles of attack tested. Specifically, this curve was obtained by deploying VG4 for angles of attack between 0 ° and 4 °, VG5 at 6 °, no VGs between 8 ° and 14 ° (this corresponds to the clean airfoil condition), and VG2 between 16 ° and 20 °, as listed in Tables 1 and 2.

By deploying different VG configurations in terms of VG height and distance from the leading edge, the lift on the wing can then be increased. Figure 7B shows the effects of the active VG configuration on the lift coefficient of the airfoil at a Reynolds number of 140,000. Like Figure 7A, it can be observed that the active device is able to deploy different VGs configuration to always achieve the maximum value of the coefficient of lift. Specifically, the black curve was obtained by deploying VG1 for angles of attack between 0° and 2°, VG2 at 4°, VG4 at 6°, VG1 at 8°, VG5 at 10°, VG4 at 12°, VG2 at angles of attack between 14° and 16°, VG5 at 18°, and VG4 at 20°, as listed in Tables 1 and 2. Results in Figure 7 show then that our device is always able to provide the maximum lift coefficient for different values of Reynolds number and angles of attack by deploying different desired VG configurations.

Conclusion

In this study, the aerodynamic performance of a NASA Langley Research Center LS (1)-0417 GA(W)-1 section airfoil equipped with active VGs powered by TSAMs was investigated at Reynolds numbers of 100,000 and 140,000. Unlike conventional passive devices, these VGs can be deployed on-demand while adapting to changing flow conditions. Initially, we explored the performance of passive VGs, experimenting with various geometries and configurations. Building on the success of our different best-performing case scenario, we designed an active device able to deploy a desired VGs configuration for different Reynolds numbers and angles of attack with the goal of achieving the maximum value of lift coefficient for different flow conditions.

Table 2. Angles of attack Vs. VG configuration deployed at Re = 140,000

Angles of attack in degrees (°)	Configuration deployed for TSAM powered VGs
0	VG1
2	VG1
4	VG2
6	VG4
8	VG1
10	VG5
12	VG4
14	VG2
16	VG2
18	VG5
20	VG5

CA, clean airfoil.

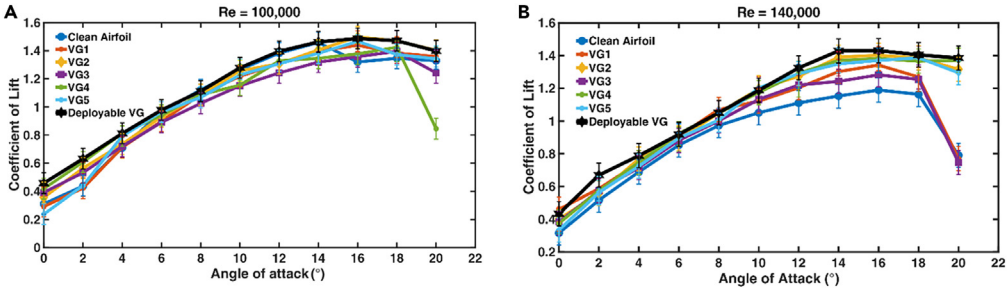

Figure 7. Effects of VGs deployed by electrothermally actuated TSAMs on the lift characteristics of the airfoil
(A) Reynolds number of 100,000 (B) Reynolds number of 140,000.

This paper demonstrated that cephalopods inspired TSAMs can be used to deploy on-demand VG configurations for flow controls, by mimicking the working mechanism and flow control performance of cephalopods' papillae, and by combining the main advantages of static and active solutions for flow controls in terms of portability and low power requirements.

While this study focused on coefficient of lift and stall angles as a simple proof of concept, it opens exciting possibilities for future investigations, including study of drag, flow visualization analysis, and linearized drag polar.

Limitations of the study

One of the biggest challenges encountered in this study was controlling the TSAMs actuation in the wind tunnel to reach the desired deployment height. As the TSAMs are heated via electrothermal actuation, the flow of air across the airfoil tends to cool them down even with continuous increase in voltage. Additionally, there is the risk of overheating and then damaging the TSAMs if the input voltage exceeds the allowed threshold value. We addressed this challenge by implementing a robust controller. However, the controller must be properly tuned according to specific flow conditions.

Another limitation was the identification of the optimal static VG configurations for achieving peak performance in terms of lift increase and stall delay that necessitated a series of experimental trials. Because of a trial-and-error process, we cannot guarantee that the configurations identified correspond to the optimal ones.

STAR★METHODS

Detailed methods are provided in the online version of this paper and include the following:

- KEY RESOURCES TABLE
- RESOURCE AVAILABILITY
  - Lead contact
  - Materials availability
  - Data and code availability
- METHOD DETAILS
  - Design and manufacturing of the airfoil and the vortex generators
  - Fabrication and modeling of the TSAMs
  - Fabrication of the active device with deployable VGs
  - Experimental facilities and design of experiments
- QUANTIFICATION AND STATISTICAL ANALYSIS
  - Control architecture

ACKNOWLEDGMENTS

This work was funded by the Office of Naval Research (Grant #N00014-22-1-2021).

AUTHOR CONTRIBUTIONS

Investigation, Methodology, Data Curation and Analysis and Writing Original Draft, R.M.; Investigation, Methodology, Data Curation and Analysis and Writing Original Draft, P.K.; Investigation and Writing Original Draft, T.W; Investigation, T.J.; Planning, Review and Editing, A.K. and J.B.; Conceptualization, Funding Acquisition, Visualization, Project Administration, Reviewing and Editing, C.L.

DECLARATION OF INTERESTS

The authors declare that they have no known competing financial interest or personal relationship that could have appeared to influence the work reported in this paper.

Received: June 14, 2023
Revised: September 18, 2023
Accepted: October 26, 2023
Published: November 2, 2023

REFERENCES

1. Laghari, A.A., Jumani, A.K., Laghari, R.A., and Nawaz, H. (2023). Unmanned aerial vehicles: A review. Cogn. Robot. *3*, 8–22. https://doi.org/10.1016/j.cogr.2022.12.004.
2. JONES, G.P., PEARLSTINE, L.G., and PERCIVAL, H.F. (2006). An Assessment of Small Unmanned Aerial Vehicles for Wildlife Research. Wildl. Soc. Bull. *34*, 750–758. https://doi.org/10.2193/0091-7648(2006)34[750:aaosua]2.0.co;2.
3. Elmore, J.A., Curran, M.F., Evans, K.O., Samiappan, S., Zhou, M., Pfeiffer, M.B., Blackwell, B.F., and Iglay, R.B. (2021). Evidence on the effectiveness of small unmanned aircraft systems (sUAS) as a survey tool for North American terrestrial, vertebrate animals: a systematic map protocol. Environ. Evid. *10*, 15–16. https://doi.org/10.1186/s13750-021-00228-w.
4. Lissaman, P.B.S. (1983). Low-Reynolds-Number Airfoils. Annu. Rev. Fluid Mech. *15*, 223–239. https://doi.org/10.1146/annurev.fl.15.010183.001255.
5. Xie, Y., Rao, Y., Cheng, Y., and Tian, W. (2022). Investigation into the laminar separation control of airfoils at low Reynolds numbers by dimple vortex generators. Aerosp. Sci. Technol. *129*, 107841. https://doi.org/10.1016/j.ast.2022.107841.
6. Yang, Z., and Hu, H. (2008). Laminar flow separation and transition on a low-Reynolds-number airfoil. J. Aircr. *45*, 1067–1070. https://doi.org/10.2514/1.35051.
7. Wang, J., and Feng, L. (2018). Vortex Generator. Flow Control Tech. Appl. 48–64. https://doi.org/10.1017/9781316676448.004.
8. Bakhtiari, M., and Ghassemi, H. (2014). Numerical Analysis of Electromagnetic Control of the Boundary Layer Flow on a Ship Hull. Open J. Fluid Dyn. *04*, 74–82. https://doi.org/10.4236/ojfd.2014.41006.
9. Godard, G., and Stanislas, M. (2006). Control of a decelerating boundary layer. Part 1: Optimization of passive vortex generators. Aerosp. Sci. Technol. *10*, 181–191. https://doi.org/10.1016/j.ast.2005.11.007.
10. Martínez-Filgueira, P., Fernandez-Gamiz, U., Zulueta, E., Errasti, I., and Fernandez-Gauna, B. (2017). Parametric study of low-profile vortex generators. Int. J. Hydrogen Energy *42*, 17700–17712.
11. Lengani, D., Simoni, D., Ubaldi, M., Zunino, P., and Bertini, F. (2011). Turbulent boundary layer separation control and loss evaluation of low profile vortex generators. Exp. Therm. Fluid Sci. *35*, 1505–1513. https://doi.org/10.1016/j.expthermflusci.2011.06.011.
12. Zhang, L., Yang, K., and Xu, J.-Z. (2010). Effects on wind turbine airfoils by vortex generators. K. Cheng Je Wu Li Hsueh Pao/Journal Eng. Thermophys. *31*, 749–752.
13. Li, X., Yang, K., and Wang, X. (2019). Experimental and numerical analysis of the effect of vortex generator height on vortex characteristics and airfoil aerodynamic performance. Energies *12*, 959. https://doi.org/10.3390/en12050959.
14. Martínez-Filgueira, P., Fernandez-Gamiz, U., Zulueta, E., Errasti, I., and Fernandez-Gauna, B. (2017). Parametric study of low-profile vortex generators. Int. J. Hydrogen Energy *42*, 17700–17712. https://doi.org/10.1016/j.ijhydene.2017.03.102.
15. Zhang, L., Li, X., Yang, K., and Xue, D. (2016). Effects of vortex generators on aerodynamic performance of thick wind turbine airfoils. J. Wind Eng. Ind. Aerodyn. *156*, 84–92. https://doi.org/10.1016/j.jweia.2016.07.013.
16. Seshagiri, A., Cooper, E., and Traub, L.W. (2009). Effects of vortex generators on an airfoil at low reynolds numbers. J. Aircr. *46*, 116–122. https://doi.org/10.2514/1.36241.
17. Xue, S., Johnson, B., Chao, D., Sareen, A., and Westergaard, C. (2010). Advanced aerodynamic modeling of vortex generators for wind turbine applications. Eur. Wind Energy Conf. Exhib. *5*, 3721–3731.
18. Forster, K.J., Barber, T.J., Diasinos, S., and Doig, G. (2017). Interactions of a counter-rotating vortex pair at multiple offsets. Exp. Therm. Fluid Sci. *86*, 63–74. https://doi.org/10.1016/j.expthermflusci.2017.04.007.
19. Velte, C.M., Hansen, M.O.L., and Cavar, D. (2008). Flow analysis of vortex generators on wing sections by stereoscopic particle image velocimetry measurements. Environ. Res. Lett. *3*, 015006. https://doi.org/10.1088/1748-9326/3/1/015006.
20. Wang, H., Zhang, B., Qiu, Q., and Xu, X. (2017). Flow control on the NREL S809 wind turbine airfoil using vortex generators. Energy *118*, 1210–1221. https://doi.org/10.1016/j.energy.2016.11.003.
21. Lee, H.M., and Kwon, O.J. (2019). Numerical Simulation of Horizontal Axis Wind Turbines with Vortex Generators. Int. J. Aeronaut. Space Sci. *20*, 325–334. https://doi.org/10.1007/s42405-018-0118-z.
22. Zhu, C., Wang, T., and Shao, T. (2019). Investigation into three-dimensional rotational effect on HAWT with numerical simulations. Taiyangneng Xuebao/Acta Energiae Solaris Sin. *40*, 1747–1755.
23. Akbarzadeh, A.M., and Borazjani, I. (2020). Controlling flow separation on a thick airfoil using backward traveling waves. AIAA J. *58*, 3799–3807. https://doi.org/10.2514/1.J059428.
24. DeMauro, E.P., Dell'Orso, H., Zaremski, S., Leong, C.M., and Amitay, M. (2015). Control of laminar separation bubble on NACA 0009 airfoil using electroactive polymers. AIAA J. *53*, 2270–2279. https://doi.org/10.2514/1.J053670.
25. Sato, M., Asada, K., Nonomura, T., Kawai, S., and Fujii, K. (2017). Large-Eddy Simulation of NACA 0015 Airfoil Flow at Reynolds Number of 1.6 × 106. AIAA J. *55*, 673–679. https://doi.org/10.2514/1.J054963.
26. Jones, G., Santer, M., Debiasi, M., and Papadakis, G. (2018). Control of flow separation around an airfoil at low Reynolds numbers using periodic surface morphing. J. Fluids Struct. *76*, 536–557. https://doi.org/10.1016/j.jfluidstructs.2017.11.008.
27. Crittenden, T.M., and Glezer, A. (2006). A high-speed, compressible synthetic jet. Phys. Fluids *18*. https://doi.org/10.1063/1.2166451.
28. Moralev, I., Sherbakova, V., Selivonin, I., Bityurin, V., and Ustinov, M. (2018). Effect of the discharge constriction in DBD plasma actuator on the laminar boundary layer. Int. J. Heat Mass Transf. *116*, 1326–1340. https://doi.org/10.1016/j.ijheatmasstransfer.2017.09.121.
29. Le Pape, A., Costes, M., Richez, F., Joubert, G., David, F., and Deluc, J.M. (2012). Dynamic stall control using deployable leading-edge vortex generators. AIAA J. *50*, 2135–2145. https://doi.org/10.2514/1.J051452.
30. Storms, B.L., and Jang, C.S. (1994). Lift enhancement of an airfoil using a Gurney flap and vortex generators. J. Aircr. *31*, 542–547. https://doi.org/10.2514/3.46528.
31. Nissle, S., Kaiser, M., Hübler, M., Gurka, M., and Breuer, U. (2018). Adaptive vortex generators based on active hybrid composites: from idea to flight test. CEAS Aeronaut. J. *9*, 661–670. https://doi.org/10.1007/s13272-018-0316-1.
32. Lamuta, C., He, H., Zhang, K., Rogalski, M., Sottos, N., and Tawfick, S. (2019). Digital Texture Voxels for Stretchable Morphing Skin Applications. Adv. Mater. Technol. *4*, 2–7. https://doi.org/10.1002/admt.201900260.
33. Allen, J.J., Bell, G.R.R., Kuzirian, A.M., and Hanlon, R.T. (2013). Cuttlefish skin papilla morphology suggests a muscular hydrostatic function for rapid changeability. J. Morphol. *274*, 645–656. https://doi.org/10.1002/jmor.20121.
34. Chiao, C.C., Chubb, C., and Hanlon, R.T. (2015). A review of visual perception mechanisms that regulate rapid adaptive camouflage in cuttlefish. J. Comp. Physiol. A Neuroethol. Sens. Neural Behav. Physiol. *201*, 933–945. https://doi.org/10.1007/s00359-015-0988-5.
35. Allen, J.J., Bell, G.R.R., Kuzirian, A.M., Velankar, S.S., and Hanlon, R.T. (2014). Comparative morphology of changeable skin papillae in octopus and cuttlefish. J. Morphol. *275*, 371–390. https://doi.org/10.1002/jmor.20221.
36. Fei, F., Kotak, P., He, L., Li, X., Vanderhoef, C., Lamuta, C., and Song, X. (2021). Cephalopod-Inspired Stretchable Self-Morphing Skin Via Embedded Printing and Twisted Spiral

Artificial Muscles. Adv. Funct. Mater. *31*, 1–11. https://doi.org/10.1002/adfm.202105528.
37. Hanlon, R. (2007). Cephalopod dynamic camouflage. Curr. Biol. *17*, 400–404. https://doi.org/10.1016/j.cub.2007.03.034.
38. Kotak, P., Weerakkody, T., and Lamuta, C. (2021). Physics-based dynamic model for the electro-thermal actuation of bio-inspired twisted spiral artificial muscles (TSAMs). Polymer (Guildf) *222*, 123642. https://doi.org/10.1016/j.polymer.2021.123642.
39. Greco, C., Kotak, P., Gallegos, J.K., Fang, J., Wilkinson, A., Pagnotta, L., and Lamuta, C. (2020). Scalable manufacturing system for bionspired twisted spiral artificial muscles (TSAMs). Manuf. Lett. *26*, 6–11. https://doi.org/10.1016/j.mfglet.2020.08.009.
40. Kotak, P., Johnson, T., and Lamuta, C. (2023). Bioinspired Fouling-Release Smart Skin Powered by Twisted Spiral Artificial Muscles (TSAMs). Adv. Mater. Technol. *8*, 2201262. https://doi.org/10.1002/admt.202201262.
41. Greco, C., Kotak, P., Pagnotta, L., and Lamuta, C. (2022). The evolution of mechanical actuation: from conventional actuators to artificial muscles. Int. Mater. Rev. *67*, 575–619. https://doi.org/10.1080/09506608.2021.1971428.
42. Godsk, K.B. (2010). Wind Turbine Blades With Vortex Generators. https://patents.google.com/patent/US7914259B2/en.
43. Zhu, C., Wang, T., Chen, J., and Zhong, W. (2020). Effect of single-row and double-row passive vortex generators on the deep dynamic stall of a wind turbine airfoil. Energies *13*, 2535. https://doi.org/10.3390/en13102535.
44. Sørensen, N.N., Zahle, F., Bak, C., and Vronsky, T. (2014). Prediction of the effect of vortex generators on airfoil performance. J. Phys. Conf. Ser. *524*, 012019. https://doi.org/10.1088/1742-6596/524/1/012019.
45. Lee, H.M., and Wu, Y. (2013). An experimental study of stall delay on the blade of a horizontal-axis wind turbine using tomographic particle image velocimetry. J. Wind Eng. Ind. Aerodyn. *123*, 56–68. https://doi.org/10.1016/j.jweia.2013.10.005.
46. Jiang, R., Zhao, Z., Liu, H., Wang, T., Chen, M., Feng, J., and Wang, D. (2022). Numerical study on the influence of vortex generators on wind turbine aerodynamic performance considering rotational effect. Renew. Energy *186*, 730–741. https://doi.org/10.1016/j.renene.2022.01.026.
47. Li, S., and Caracoglia, L. (2020). Experimental error examination and its effects on the aerodynamic properties of wind turbine blades. J. Wind Eng. Ind. Aerodyn. *206*, 104357. https://doi.org/10.1016/j.jweia.2020.104357.
48. Kirk, T.M., and Yarusevych, S. (2017). Vortex shedding within laminar separation bubbles forming over an airfoil. Exp. Fluids *58*, 43. https://doi.org/10.1007/s00348-017-2308-z.
49. Liu, Y., Li, P., He, W., and Jiang, K. (2020). Numerical study of the effect of surface grooves on the aerodynamic performance of a NACA 4415 airfoil for small wind turbines. J. Wind Eng. Ind. Aerodyn. *206*, 104263. https://doi.org/10.1016/j.jweia.2020.104263.
50. Zhao, Z., Jiang, R., Feng, J., Liu, H., Wang, T., Shen, W., Chen, M., Wang, D., and Liu, Y. (2022). Researches on vortex generators applied to wind turbines: A review. Ocean Eng *253*, 111266. https://doi.org/10.1016/j.oceaneng.2022.111266.
51. Zhao, Z., Chen, M., Liu, H., Wang, T., and Xu, B. (2021). Research on parametric modeling methods for vortex generators on flat plate. J. Renew. Sustain. Energy *13*. https://doi.org/10.1063/5.0030143.
52. Baldacchino, D., Ferreira, C., Tavernier, D.D., Timmer, W.A., and van Bussel, G.J.W. (2018). Experimental parameter study for passive vortex generators on a 30% thick airfoil. Wind Energy *21*, 745–765. https://doi.org/10.1002/we.2191.
53. Haines, C.S., Lima, M.D., Li, N., Spinks, G.M., Foroughi, J., Madden, J.D.W., Kim, S.H., Fang, S., Jung de Andrade, M., Göktepe, F., et al. (2014). Artificial muscles from fishing line and sewing thread. Science *343*, 868–872. https://doi.org/10.1126/science.1246906.
54. Winslow, J., Otsuka, H., Govindarajan, B., and Chopra, I. (2018). Basic understanding of airfoil characteristics at low Reynolds numbers (104–105). J. Aircr. *55*, 1050–1061. https://doi.org/10.2514/1.C034415.
55. Karnjanaparichat, T., and Pongvuthithum, R. (2017). Adaptive tracking control of multi-link robots actuated by pneumatic muscles with additive disturbances. Robotica *35*, 2139–2156. https://doi.org/10.1017/S0263574716000758.
56. Weerakkody, T.H., Hammond, M., Neilan, J.H., Cichella, V., and Lamuta, C. (2023). Modeling and control of twisted and coiled artificial muscles for soft robotics. Meccanica *58*, 643–658. https://doi.org/10.1007/s11012-023-01651-8.
57. Hammond, M., Cichella, V., Weerakkody, T., and Lamuta, C. (2022). Robust and Adaptive Sampled-Data Control of Twisted and Coiled Artificial Muscles. IEEE Control Syst. Lett. *6*, 1232–1237. https://doi.org/10.1109/LCSYS.2021.3091414.
58. Giovinco, V., Kotak, P., Cichella, V., Maletta, C., and Lamuta, C. (2020). Dynamic model for the tensile actuation of thermally and electro-thermally actuated twisted and coiled artificial muscles (TCAMs). Smart Mater. Struct. *29*, 025004. https://doi.org/10.1088/1361-665X/ab5e38.

STAR★METHODS

KEY RESOURCES TABLE

REAGENT or RESOURCE	SOURCE	IDENTIFIER
Chemicals, peptides, and recombinant proteins		
Polylactic acid (PLA)	RAISE3D, Irvine, CA, USA	#2207300098
Photopolymer resin (Rigid 4000)	Formlabs Inc, Somerville, Massachusetts, USA	RS-F2-GPBK-04
Isopropyl alcohol	Sigma-Aldrich, GmBh	#1003500617
Thermally conductive epoxy adhesive	MG Chemicals Ltd. Ontario, Canada	#8329TCM-6ML
Deposited data		
Angle of vs. VG configuration deployed	See Tables 1 and 2	N/A
Vortex generators configurations	See STAR methods	N/A
Repeatability of measured data	See STAR methods	N/A
Software and algorithms		
MATLAB R2023a	Mathworks	https://www.mathworks.com/products/new_products/r2023a-transition.html
Other		
36 AWG Copper wire	Remington Industries, USA	MW 79-C
PVDF nylon fishing line	KastKing Kovert, USA	#X001GH5DU9
Formlabs 3D printer	Formlabs Inc, Somerville, Massachusetts, USA	Form 3B+
Raise 3D printer	RAISE3D, Irvine, CA, USA	N/A
Wind tunnel facility	University of Iowa fluids laboratory	N/A
Mitutoyo 3600 digital protractor	Mitutoyo corporation, Illinois, USA	Pro 360, 950-317, SN: 22100543
Thermistor	Mouser Electronics, Texas, USA	#GA10K3A1B

RESOURCE AVAILABILITY

Lead contact

Further information and requests and reagents should be directed to and will be fulfilled by the lead contact, Caterina Lamuta (caterina-lamuta@uiowa.edu).

Materials availability

This study does not generate new unique reagents.

Data and code availability

- All raw unprocessed data obtained during the experiments are available from the lead contact upon request.
- This paper does not report original code.
- Any additional information required to reanalyze the data reported in this paper is available from the lead contact upon request.

METHOD DETAILS

Design and manufacturing of the airfoil and the vortex generators

The airfoil adopted in the experiments is a NASA Langley Research Center LS (1)- 0417 GA(W)-1 section with a chord of 330 mm and 203.2 mm span.[16] As depicted in the below image, the airfoil was designed in PTC Creo – 9.0.3.0 software and fabricated using a polylactic acid (PLA) via fused deposition modeling (FDM) 3D printing technique. To facilitate the installation of both the static and deployable VGs, a two-part prototype airfoil was designed. The prototype is comprised of a nose (see below image) and a receiver section (both sections are shown in below the image). The nose section extends from the leading edge of the airfoil up to a length of 50 mm along the chord. This design allows for switching out the airfoil nose to accommodate various VG configurations, as well as deployable VGs, without requiring removal of the airfoil receiver.

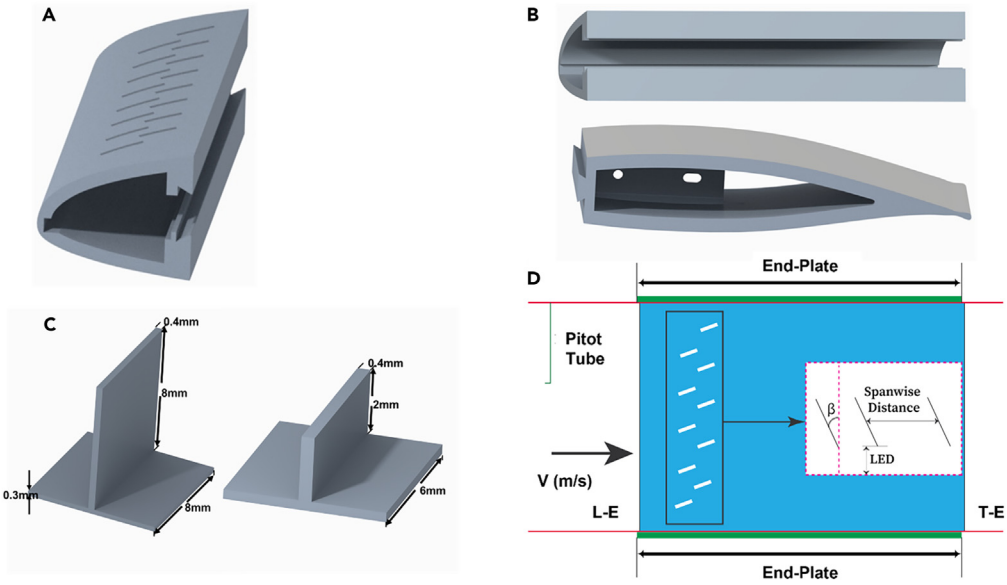

Design of the airfoil and VGs

(A) Nose section of the airfoil revealing the groove for the deployment of the VGs.

(B) Rear view of the nose section of the airfoil for the incorporation of the dynamic device and the receiving end.

(C) Static vortex generators for experimental trials (VG_B for the big VGs and VG_S for the small VGs).

(D) Sketch of model installation: L-E, leading edge; TE, trailing edge; LED, leading edge distance, β; orientation.

As highlighted in the previous section, in order to achieve optimum performance from VGs, their geometry and configuration in terms of height, distance from leading edge, span-wise distance, number of rows and orientation with respect to the leading edge must be carefully chosen.[15,20,50] This is usually achieved via computational simulations or experimental tests.[15,16,51,52] In this study, different geometries and configurations of vortex generators were experimentally tested in the wind tunnel to identify the optimal configurations for different flow conditions. The VGs were fabricated using a photopolymer resin via a stereolithography (SLA) 3D printing technique. After 3D printing, the VGs are washed in an isopropyl alcohol bath for 20 min to remove any uncured resin and cured in an oven for 20 min at 60 $^{\circ}C$ to achieve maximum strength and stability. After several experiments in the wind tunnel with 3D printed static VGs with different geometry, the two geometries depicted in above the image were finally adopted since they exhibit better results in terms of lift generation and stall delay at different Reynolds number and angles of attack. A schematic layout of the VGs configuration in terms of orientation and distance from the leading edge is also depicted in above the image.

Fabrication and modeling of the TSAMs

As detailed in,[38,53] the TSAMs used in this study were fabricated from inexpensive polyvinylidene fluoride (PVDF) fishing lines (KastKing Kovert Fluorocarbon fishing line, KastKing, USA, $\varnothing = 0.7$ mm) with an initial length of 70 cm. An Arduino controlled stepper motor was used to apply a pre-twist to the fishing line while simultaneously wrapping an insulated 36 AWG copper wire (Remington Industries, USA) around it to provide an electrothermal actuation of the muscle. Upon achieving a length of 18 cm of the copper/PVDF electrically conducting composite, 240 twists were further applied until the onset of a spontaneous coiling. The resulting composite was guided into an adhesive substrate to obtain about five continuous flat coils and then annealed under a constant weight of 3 kg for 2*hrs* at 135$^{\circ}C$ to retain the final flat spiral shape. The inner coil has a diameter of 3 mm while the outer coil has a diameter of 16 mm. As depicted in Figure 2C in the previous section, the TSAM exhibits the shape changing ability of an octopi papillae skin muscle upon activation by providing a large vertical displacement. The actuation can be attributed to an anisotropic volume expansion in the radial direction resulting in an internal untwisting and uncoiling of the spiral which then results in an out of plane vertical displacement.[32]

Previously developed dynamic and static models[32,38] explain how the actuation mechanism of TSAMs can be summarized in three main steps. The first step in the model relates the input voltage and actuation time to the temperature attained $T(t)$ upon Joule heating, as described in Equation 2.

$$C_t \dot{T}(t) = \frac{V(t)^2}{R} - h(t)A(t)(T(t) - T_{amb}) \quad \text{(Equation 2)}$$

where R is the electrical resistance of the TSAMs, $V(t)$ is the input voltage that provides the actuation, C_t is the thermal mass of the TSAM, $h(t)$ is the heat transfer coefficient between air and TSAM, $A(t)$ is the total area of the TSAM exposed to cooling and T_{amb} is the ambient room temperature.

The second step relates the radial expansion of the TSAM to the rise in temperature through the coefficient of thermal expansion using Equation 3.

$$d_i(t) = \Delta T d_0 CTE(t) + d_0 \quad \text{(Equation 3)}$$

where $d_i(t)$ is the radial expansion of the TSAM, $CTE(t)$ is the coefficient of thermal expansion, d_0 is the initial fiber diameter and $\Delta T = T(t) - T_{amb}$.

The final step gives a theoretical expression for the output vertical displacement of the TSAM as a function of the radial expansion of the fiber.

$$(m + m_1)\ddot{x}_w(t) + \frac{\frac{\pi d_i(t)^4}{4}\eta}{\frac{(D_1^2+D_2^2)n_0}{4D_2K_W}\left(1 - \frac{d_0}{d_i(t)}\right) - \frac{2n_a(D_1^2+D_2^2)(D_1+D_2)W}{Gd_i(t)^4}}\dot{x}_w(t) + \frac{mg+W}{\frac{(D_1^2+D_2^2)n_0}{4D_2K_W}\left(1 - \frac{d_0}{d_i(t)}\right) - \frac{2n_a(D_1^2+D_2^2)(D_1+D_2)W}{Gd_i(t)^4}}x_w(t) = mg + W \quad \text{(Equation 4)}$$

Where, W is the external weight applied to the TSAM (i.e., VG weight for the device proposed in this work), m is the TSAM's mass, m_1 is the mass of the external compression load (in the case, VGs), $x(t)$ is the vertical displacement, m is the mass of the TSAM, η is the viscosity of the TSAM fiber, D_1 is the inner spiral diameter of the TSAM, D_2 is the outer spiral diameter of the TSAM, n_0 is the number of turns inserted during twisting, K_W is Wahl's curvature correction factor, n_a is the number of spirals in the TSAM, and G is the shear modulus of the PVDF fiber. The TSAM was modeled as a second-order spring-mass-damper system to obtain the model summarized above.[36]

Fabrication of the active device with deployable VGs

Active flow control devices as referred to in this study consist of arrays of two VGs mounted on a single TSAM such that upon actuation they protrude out of the groove in the airfoil nose (shown in Figure 6D). A single TSAM can deploy two VGs at a time. The starting procedure for the development of the active device involves 3D printing a flat rectangular insert plate (L = 203.2 mm, W = 46 mm, H = 2.47 mm) with dimensions carefully tailored to fit into the rear portion of the nose section of the airfoil. Eight TSAMs were mounted on the plates using a hot-melt adhesive while a total of 16 VGs were mounted on the topmost spiral of the TSAMs with fast-curing silicone elastomer as depicted in Figure 6B. In this study, a fully deployable system of VGs, powered by TSAMs, comprises a total of sixteen VGs and eight TSAMs, arranged in two rows. This arrangement forms a single deployable active flow control device that underwent testing in our research.

The electrothermal actuation of the dynamic devices was achieved using a DC power supply through a microcontroller and NPN transistor. The overall control circuitry was embedded inside the hollow section of the receiving end of the airfoil (Figure 6C). Before electrothermal actuation, the TSAMs and VGs are in an initial flat state and embedded inside the airfoil's nose section. Once actuated, the TSAMs move vertically, causing the VGs to deploy through the nose groove (Figure 6D) into the incoming free stream of air, thereby promoting boundary-layer transition and enhancing the overall aerodynamic performance.

Experimental facilities and design of experiments

The experiments were carried out at the University of Iowa Fluids Workshop. The angle of attack of the wing was measured using a Mitutoyo 3600 digital protractor, which has a resolution of 0.01° in accordance with the manufacturer's specifications. Two splitter plates with dimensions of 2.5c were mounted at either extremity of the airfoil span in the test section with a clearance of $\frac{d}{c} = 0.15$ where d is the distance between one extremity of the airfoil and splitter plate (Figure 4A). The splitter plates help simulate 2D quasi flow and prevent the formation of tip vortices which could interfere with flow of air on the surface of the airfoil and cause inaccurate measurements in lift force. A pitot tube attached to a pressure transducer (model PX653–05D5V from Omega Engineering Incorporation, Norwalk, Connecticut, USA) measures the dynamic pressure of the flow upstream of the airfoil. The velocity of the test section was kept at 4.59 m/s and 6.43 m/s (corresponding to a Reynolds number of 100,000 and 140,000 based on the airfoil chord length) respectively for two different experimental runs. These Reynolds number were selected because they lie within the operating range of small UAVs.[54] Two SM S-type load cells (Interface force measurement solutions, Scottsdale, Arizona, USA) with a maximum load capacity of 50N in the lift direction and a sensitivity of $\approx$ 3.0 mV/V were used in measuring lift forces. Analogue output signals from the load cells were amplified using SGA AC/DC signal amplifiers (Interface force measurement solutions, Scottsdale, Arizona, USA). Excitation voltage of 10 V Signals were transmitted from the amplifiers to NI BNC-2110 data acquisition system (National Instruments, Texas, USA). Output voltages from the data acquisition system were collected using a LabView program and then exported to MATLAB for further analysis.

To conduct experiments on passive VGs without the use of TSAMs, two rows of VGs, designated as Row 1 and Row 2, were placed on the wing. Row 1 is positioned at 20 mm from the leading edge (LE) and 25 mm from one end of the wing, with a spanwise spacing of 20 mm.

Meanwhile, Row 2 was situated at 35 mm from the LE and 40 mm from one end of the wing, with the same spanwise spacing of 20 mm (Figures 4D and 4E). The study assesses five distinct VG configurations by interchanging VGs with heights of 8 mm and 2 mm between the two rows. The table below depicts the layout of VG configurations adopted for this study. These configurations were selected as the most

effective in terms of stall delay and lift increase, after several experimental tests which included more than 20 different configurations (where the main four parameters listed in Table 1 were varied).

VG configurations	Distance from leading edge (x/c)[a]	Spanwise distance between VGs x/c	β (°)	Number of rows
VG1	0.06 for VG_B	0.06	15 °	Single row
VG2	0.06 for VG_B and 0.1for VG_S	0.06	15 °	Double row of VG_B and smaller VG_S
VG3	0.1 for VG_S	0.06	15 °	Single row VG_S
VG4	0.06 and 0.1 for VG_B	0.06	15 °	Double rows of VG_B
VG5	0.06 for VG_S and 0.1 for VG_B	0.06	15 °	Double rows of VG_S and VG_B

[a]VG_B: Big VGs with dimensions 8 mm × 0.4 mm x 8 mm; VG_S: Small VGs with dimensions 6 mm × 0.4 mm × 2 mm.

QUANTIFICATION AND STATISTICAL ANALYSIS

To validate the repeatability of the measured data using our experimental setup at Re = 100,000 and 140,000, three experimental runs were performed at each angle of attack. The relative standard deviation (RSD) was used to quantify the repeatability of the data at each angle of attack. RSD is a statistical measure used to assess the variability of data relative to its mean. It is expressed as a percentage and calculated by dividing the standard deviation by the mean, then multiplying by 100. The result on the outcome of this test is depicted in the table below. As expected, higher RSD values are measured for higher angles of attack, due to increased fluctuations.

Re = 100,000		Re = 140,000	
α^o	%RSD[a]	α^o	%RSD[b]
0	2.91	0	4.34
2	3.37	2	4.59
4	3.75	4	4.66
6	3.64	6	4.17
8	3.68	8	3.62
10	4.31	10	6.15
12	4.71	12	7.05
14	5.09	14	8.34
16	5.25	16	7.39
18	5.59	18	8.19
20	5.61	20	9.68

[a]RDS values for C_L measurements at different angles of attack at $Re = 100,000$.
[b]RDS values for C_L measurements at different angles of attack at $Re = 140,000$.

To obtain the calibration curve for lift force measurement, a direct approach was employed whereby known masses were added to the top surface of the airfoil, and the output voltage readings from the strain gauges were performed using LabView. For an average output voltage of 0.375 V determined from the lift calibration, the corresponding level of uncertainties was determined to be ± 0.074 at 95% level of significance. The resulting data was used to generate a calibration curve, allowing for accurate lift force measurements to be obtained.

Control architecture

A robust $\mathscr{L}_1$ adaptive controller[55,56] was used to control TSAMs actuation and guarantee a desired actuation temperature, considering environmental uncertainties. The temperature feedback for the proposed controller was provided by a micro thermistor attached to each TSAMs using conductive thermal paste that ensured a sufficient transfer of heat from the TSAMs to the thermistor. By adjusting the actuation temperature of each TSAM using the adaptive controller we can accurately control the TSMAs vertical displacement and then the vertical deployment of each VG. Furthermore, using the controller, VGs can be held at a given height without overheating the TSAMs thereby allowing for the flow to settle over the airfoil.

In previous works we proposed a displacement feedback controller with a temperature observer for Twisted and Coiled Artificial Muscles (TCAMs).[56–58]

The results have shown that $\mathscr{L}_1$ adaptive control can avoid overheating and withstand any environmental uncertainties during the actuation of bioinspired artificial muscles. The controller is here extended to TSAMs.

The second-order dynamic equation governing the TSAM motion can be simplified from Equation 4 as follows:

$$m\ddot{\ell}(t) + b\dot{\ell}(t) + k\ell(t) = F_e \quad \text{(Equation 5)}$$

where $F_e = mg + W$ is an external force applied on the TSAM, m is the total mass of the system, b and k are damping and spring coefficients of the TSAM, and ℓ is the TSAMs length. In,[38] it was shown that both the damping and spring coefficients are a function of temperature T_Δ: i.e., $b \triangleq b(T_\Delta)$ and $k \triangleq k(T_\Delta)$.

Then,

$$b(T_\Delta) = \frac{\eta A_s k(T_\Delta)}{F_e}$$

$$k(T_\Delta) = \frac{mg+W}{\left[\frac{(D_1^2+D_2^2)n_0}{4D_2K_w}\left(1 - \frac{d_0}{d_i(t)}\right)\right]}. \quad \text{(Equation 6)}$$

Here, η is the viscosity of the TSAM polymer fiber. During the actuation, $b_\Delta = b(T_\Delta) - \overline{b}$ where $\overline{b} = b(0)$ is the damping coefficient when $T_\Delta = 0$. Similarly, the stiffness also can be written as $k_\Delta = k(T_\Delta) - \overline{k}$ with $\overline{k} = k(0)$. Then we can rewrite the dynamic equation as

$$m\ddot{\ell}(t) + \overline{b}\dot{\ell}(t) + \overline{k}\ell(t) = mg + W - b_\Delta\dot{\ell}(t) - k_\Delta\ell(t). \quad \text{(Equation 7)}$$

The right-hand side of the equation can be approximated to a linear relationship as

$$cT_\Delta(t) \approx mg + W - b_\Delta\dot{\ell}(t) - k_\Delta\ell(t), \quad \text{(Equation 8)}$$

for some $c > 0$. The system of equations can be presented as a state-space model that consists of both linear and nonlinear, as in

$$\dot{x}(t) = A_p x(t) + B_p u(t) + f(x, x(t)),$$

$$y(t) = C_p x(t), \quad \text{(Equation 9)}$$

where (A_p, B_p, C_p) are realization triplets with state vector $x(t) = [\ell(t) \quad \dot{\ell}(t) \quad T_\Delta(t)]^\top$, input $u(t) = V^2(t) - \frac{V_{max}^2}{2}$ with V_{max} is the maximum supply voltage to the system, and output $y(t) = d(t)$.

Any unknown time-varying nonlinear functions that accounted for system uncertainties are represented in $f(t, x(t))$. With the dynamic equations mentioned above, the realization triplets can be expressed as

$$A_p = \begin{bmatrix} 0 & 1 & 0 \\ -\frac{\overline{k}}{m} & -\frac{\overline{b}}{m} & \frac{c}{m} \\ 0 & 0 & -\frac{\overline{h}\overline{A}_s}{m} \end{bmatrix},$$

$$B_p = \begin{bmatrix} 0 \\ 0 \\ \frac{1}{C_t R} \end{bmatrix}, C_p = [1 \quad 0 \quad 0]. \quad \text{(Equation 10)}$$

Here, $\overline{h} = h(0)$ and $\overline{A}_s = A_s(0)$ are the initial conditions of heat transfer coefficient and cross-section area of the TSAM affecting convection when $T_\Delta = 0$.

The controller architecture is shown in the below image. The temperature requirement for each TSAM was determined based on our previously published physics-based model.[38] Then that temperature was used as a desired input to the $\mathcal{L}_1$ adaptive controller. The controller determines the desired voltage for the actuation based on Equations 5, 6, 7, and 8. The real-time temperature of the TSAM was measured using a thermistor by measuring the change of resistance. This actual temperature measurement was used as feedback to the controller to maintain the position of the TSAM.

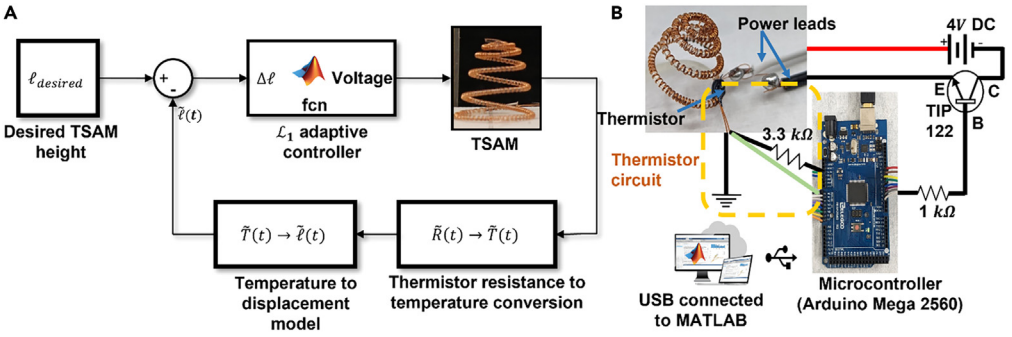

Control diagram and hardware

(A) The control architecture for position controlling of a single TSAM.

(B) The hardware setup for TSAM actuation.

The above image shows the hardware used to control a single TSAM. A thermistor was attached to the TSAM using a thermal paste. As the temperature changes, the resistance of the thermistor changes.

The resistance was measured via a voltage divider circuit as a digital voltage ($0 - 5V$) using a microcontroller analog input port. Then the voltage measurement was converted back to the resistance in the algorithm and converted into the temperature based on thermistor specifications. Upon the temperature requirement, the voltage was provided to the TSAM from a DC power source ($0 - 4V$) and the supply voltage was controlled by a pulse width modulation (PWM) signal provided by the microcontroller connected to the Darlington pair transistor *(TIP 122)*. A maximum supply voltage of $4V$ was used to avoid thermal degradation of TSAMs due to overheating. The microcontroller was connected to the CPU via a USB, and MATLAB/Simulink was used to implement the control algorithm and data acquisition. The TSAM displacement was calculated based on the temperature measured by the thermistors, and the static and dynamic models developed in our previous work.[38,56] The below image depicts the displacement and voltage plots for two TSAMs maintained at different heights using the adaptive controller. TSAM 1 in the below image is actuated and maintained at a height of 8 mm (corresponding to an actuation voltage of 4 V, as shown in the right plot). The below image depicts TSAM 2 in row 2 maintained at a height of 2 mm (corresponding to an actuation voltage of 4 V, as shown in the plot on the right). TSAM 1 and TSAM 2 actuate VG_B and VG_S (dimensions are shown in the image, p. 11), respectively.

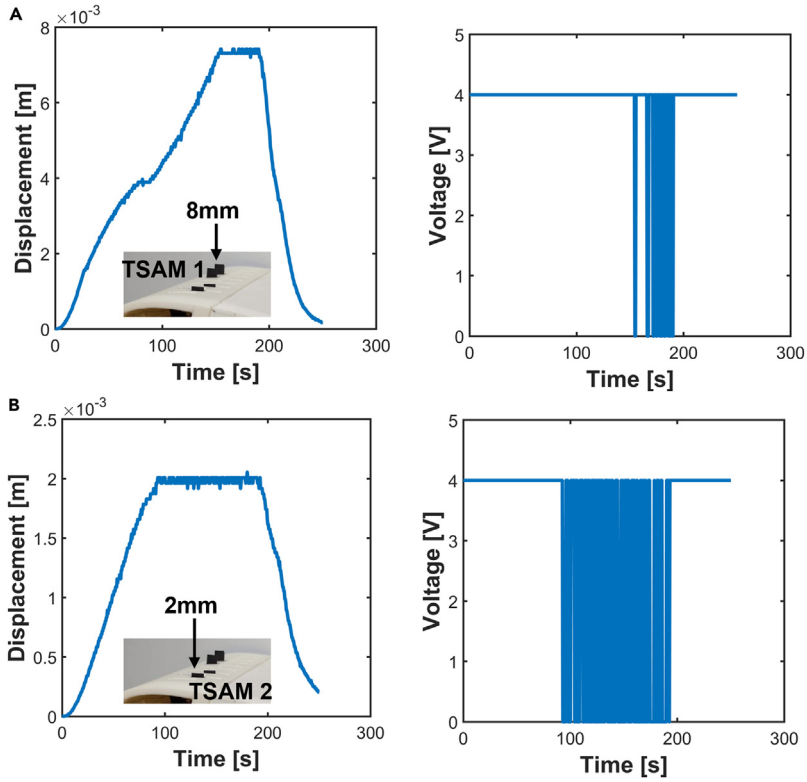

Displacement (left) and voltage (right) plots for two TSAMs actuated to and maintained at different heights using the $\mathcal{L}_1$ controller

(A and B) Row (A) refers to TSAM 1 actuating VG_B, while row (B) refers to TSAM 2 actuating VG_S, as shown in the insets.